

# Improving real-time ultrasound spine imaging with a large-aperture array

Ning Lu<sup>1</sup>, Josquin Foiret<sup>1</sup>, Yutong Guo<sup>1</sup>, Byung Chul Yoon<sup>1,2\*</sup>, Katherine W. Ferrara<sup>1\*</sup>

Ultrasound offers a safe, low-cost alternative to computed tomography (CT) and magnetic resonance imaging for spinal diagnostics and intervention by enabling real-time imaging. However, the complex structure of the spine and acoustic shadowing from bones present challenges for ultrasonography. This study addresses these limitations using an 8.8-centimeter 384-element large-aperture array and full aperture-based imaging protocols. Volumetric scanning across multiple vertebrae was accomplished in 5 seconds using ultrafast, diverging wave acquisition. In seven healthy volunteers, the large-aperture array and diverging wave transmission improved resolution, contrast, and visualization of the spinal canal, venous plexuses, and facet joints compared with conventional probes. A comparison between the coregistered CT and ultrasound scan confirmed the imaging accuracy. A simulated lumbar puncture demonstrated needle tip visualization throughout the trajectory into the spinal canal. The results suggest that large-aperture arrays, coupled with diverging wave imaging sequences, are a valuable tool for spine imaging and image-guided intervention.

Copyright © 2025 The Authors, some rights reserved; exclusive licensee American Association for the Advancement of Science. No claim to original U.S. Government Works. Distributed under a Creative Commons Attribution NonCommercial License 4.0 (CC BY-NC).

## INTRODUCTION

Imaging plays a major role in the diagnosis and treatment of various spine conditions including infection, inflammation, neoplasm, congenital abnormalities, and degenerative diseases (1). The current mainstay modalities for spine imaging are radiographs, computed tomography (CT), and magnetic resonance imaging (MRI), but there are limitations when using these modalities for diagnosis and interventional guidance. The spine is a flexible structure, and abnormalities such as nerve root compression can be positional (2), requiring dynamic imaging. However, dynamic imaging is limited with CT and MRI due to limited space and positioning within the scanner. Additional dynamic imaging flexibility is achievable with radiography or fluoroscopy, but each requires ionizing radiation and is relatively poor for evaluating soft tissues. MRI-guided procedures are not as accessible and may not be an option for patients with metal, implants, or claustrophobia. Some procedures such as lumbar puncture may be performed with manual palpation alone, but this may not be feasible in patients with a large body habitus or advanced degenerative changes.

Ultrasound is an attractive modality for spine imaging as it allows dynamic, real-time imaging of the spine in any position without ionizing radiation or a magnetic field. Recent studies have shown that ultrasound imaging can facilitate the performance of procedures by safely revealing anatomy that is difficult to obtain solely with physical examination (3–6). However, ultrasound imaging of deeper targets such as the spinal canal remains a challenging task. The acoustic impedance mismatch between bone and soft tissue substantially attenuates the acoustic intensity and limits the penetration depth. Acoustic aberration through heterogeneous tissue on the propagation path further degrades the image quality. Consequently, the spinal canal and other features deep to the spinous processes are often not visible on conventional ultrasound. Moreover, conventional ultrasound images can be difficult to assess because of

a restricted field of view (FOV) that is often smaller than the object of interest, view-dependent artifacts, and limited resolution. The lateral resolution achieved at a depth of interest is inversely proportional to the *F*-number (the depth-to-aperture ratio) (7), i.e., at a given depth, a large *F*-number (small aperture) reduces the resolving power (Fig. 1A). Therefore, small-aperture probes that are used clinically are likely to suffer from poor image quality for deep targets, particularly in obese patients (8, 9).

Large-aperture arrays offer a large FOV and improve resolution and contrast by reducing the *F*-number (10–13). In addition, the use of half-wavelength or finer pitch in a large-aperture phased array maintains high spatial resolution as a function of depth (Fig. 1A). In a conventional focused beam imaging sequence, a small subset of elements is used to form a focused beam, and such sub-aperture can be translated from one side of the array to the other to insonify a lateral range of locations without angular steering. This is often referred to as the “ray-line” method. However, the acquisition time for the ray-line sequence increases linearly with the number of elements, thus limiting the frame rate of imaging with large-aperture arrays. Advances in high-throughput ultrasound systems have enabled full control over a high number of channels (14), allowing parallel transmissions using plane waves (PW) or diverging waves (DW) to achieve image quality comparable to conventional focused beams but at video frame rates on the order of kilohertz by coherent compounding (15, 16). Furthermore, parallel sub-aperture beam-forming with graphics processing units (GPU) postprocessing on distributed systems enables high-resolution structural and functional imaging at video rates. Combining the use of a large aperture, the ultrafast imaging sequence, and the parallel processing technique improves image quality in a wide FOV at a high frame rate for applications such as musculoskeletal and liver imaging (11, 15, 17).

In this work, we present a panoramic ultrasound system combining a large-aperture array and ultrafast imaging sequence to image the human spine dynamically. The proposed system improves the imaging of spinal structures in the following manner:

1) Expanded lateral view: The combination of DW transmission and large aperture offers an expanded lateral view that visualizes three to four vertebrae in a single view in the longitudinal plane and

<sup>1</sup>Department of Radiology, Stanford University, Palo Alto, CA, USA. <sup>2</sup>Radiology Service, Veterans Affairs Palo Alto Healthcare System, Palo Alto, CA, USA.

\*Corresponding author. Email: kwferrara@stanford.edu (K.W.F.); byoon@stanford.edu (B.C.Y.)

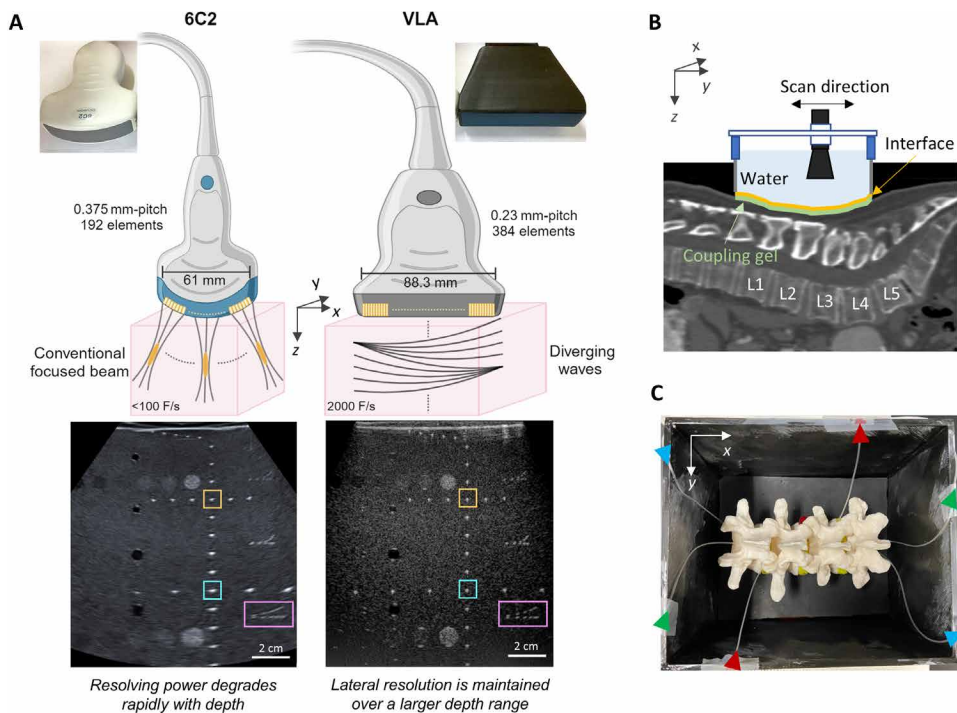


**Fig. 1. Large-aperture ultrasound array and the experimental setup.** (A) Comparison of a conventional curvilinear probe 6C2 (left) and the very large array (VLA) phased array (right). B-mode image quality was calibrated with a standard ultrasound phantom (CIRS Model 040GSE). Commercial probes are typically used with conventional focused beams, where the lateral resolution degrades rapidly as the imaging depth increases. We present the VLA array used with diverging wave (DW) transmissions, which maintains lateral resolution over a larger depth range. The schematic was created in BioRender by the authors. x axis: azimuth; y axis: elevation; z axis: depth. (B) Diagram of human volumetric spine scan setup. A coupling frame with a thin conformable rubber membrane is placed on the volunteers' lower back, and the membrane-skin interface is coupled with ultrasound gel. The VLA array is attached to a rigid rail on the frame in the transverse view, and the frame is filled with degassed water to couple between the membrane and the array surface. Such a rigid frame minimizes air bubbles at the skin/water-bath interface and offers stable acoustic coupling. The B-mode images shown in (A) are oriented in the x-z plane (into/out of paper) in (B). (C) Photo of the spine phantom for interventional procedures (tissue-mimicking background substrate not presented). Colored triangles indicate the inlet and outlet of the three tubes embedded in the spine phantom for contrast agent injection.

structures distal to the midline, such as the transverse processes on both sides in the transverse plane.

2) Enhanced resolution and contrast at an extended imaging depth: The spinal canal can be visualized with a contrast of up to 21.9 dB.

3) Anatomical measurements: Visualizing the anatomical features allows measurements of the dimensions of the vertebrae, which are important for interventional guidance and diagnosis.

4) Real-time guidance: Guiding the lumbar puncture by tracking needle insertion and extraction is feasible with a high frame rate during interventional procedures.

This combination holds promise for improved ultrasound diagnostic imaging and orthopedic procedural guidance.

## RESULTS

### DW transmission improves image quality in a large FOV

We first evaluated the performance of various imaging sequences for a very large aperture (VLA) array in a standard ultrasound phantom and a tissue-mimicking spine phantom. Because the transmission pattern determines the spatial distribution of the acoustic intensity, it directly affects the FOV, image quality, and dynamic range. We consider three transmission patterns for coherent compounding in ultrafast imaging: DW, PW, and converging waves (CW; i.e., focused beams with angular steering). These protocols steer the beam

to sample unique angular sections of  $k$ -space but with different locations of the virtual sources (18).

To quantify the spatial extent of the transmitted intensity, we define transmission angular coverage as the angle between the boundary of the transmission apodization mask and the transducer surface (Fig. 2A). Given the transmission aperture  $L$  and the maximal steering angle  $\alpha$ , the angular coverage of  $PW \pm \theta_{PW}$  is calculated as

$$\theta_{PW} = \frac{\pi}{2} + \alpha \quad (1)$$

Similarly, for DW, the transmission angular coverage of  $\pm \theta_{DW}$  is calculated as

$$\theta_{DW} = \frac{\pi}{2} + \arctan\left(\frac{r \sin \alpha + L/2}{r \cos \alpha}\right) \quad (2)$$

where  $r$  denotes the virtual source radius.

For CW, the transmission angular coverage  $\pm \theta_{CW}$  is calculated as

$$\theta_{CW} = \begin{cases} \arctan\left(\left|\frac{r \cos \alpha}{-r \sin \alpha + L/2}\right|\right) & \text{when } r < \frac{L}{2 \sin \alpha} \\ \frac{\pi}{2} & \text{when } r = \frac{L}{2 \sin \alpha} \\ \pi - \arctan\left(\frac{r \cos \alpha}{r \sin \alpha - L/2}\right) & \text{when } r > \frac{L}{2 \sin \alpha} \end{cases} \quad (3)$$

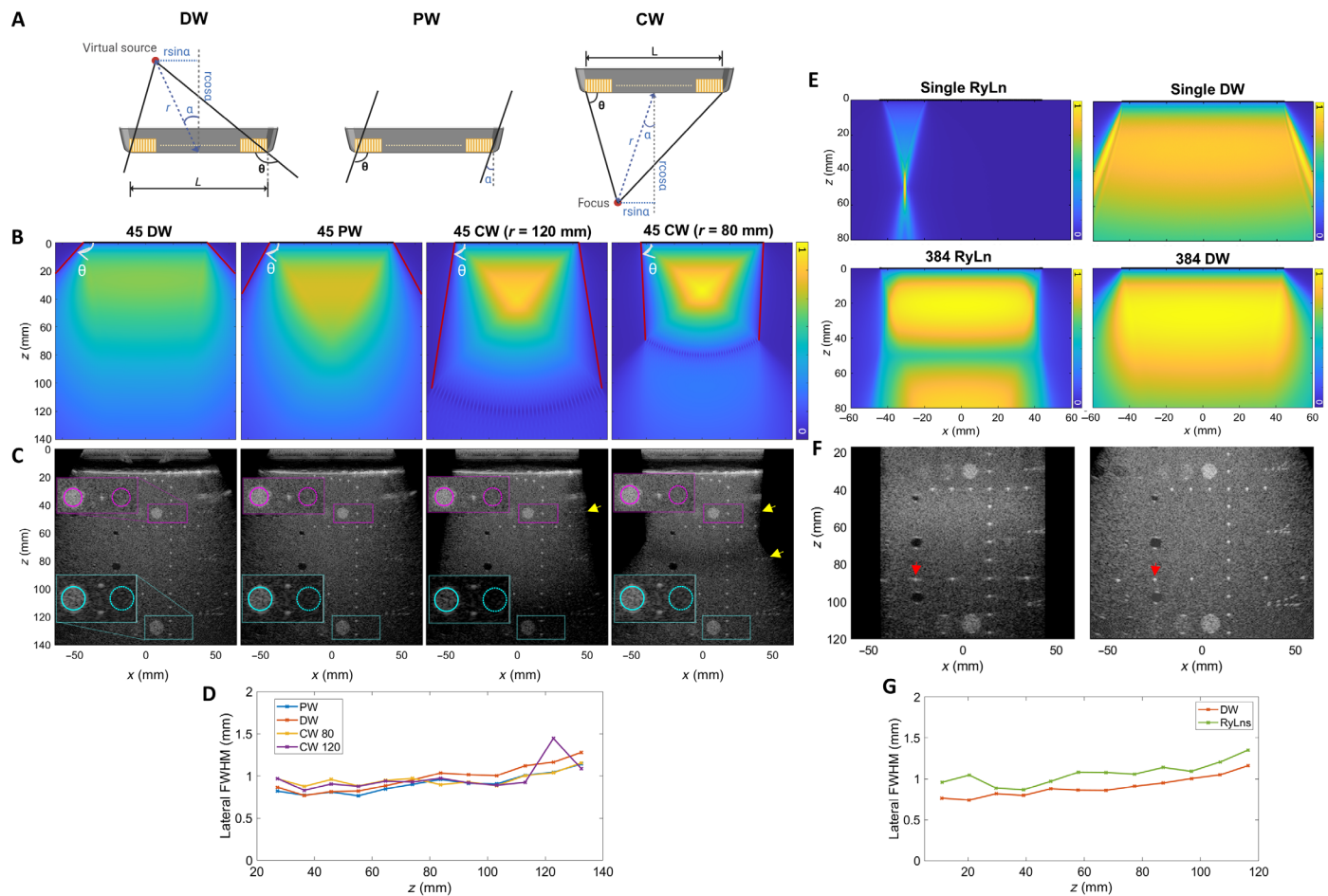


**Fig. 2. Comparison of different transmission sequences.** (A) Schematic representation of the transmission angular coverage. (B) Transmission intensity map of coherent compounding sequences simulated by the Verasonics software package. In each sequence, single-cycle pulses were transmitted 45 times with the entire aperture of the VLA array (using all 384 elements). The red lines show the boundaries of angular coverage. (C) Tissue-mimicking phantom images with no aberration. Solid and dashed circles denote the corresponding pairs of signal and background ROIs where the contrast metrics were examined in Table 2. A layer of agarose gel (~1.5 cm, sound speed = 1540 m/s) was placed between the array and the CIRS phantom for acoustic coupling. Dynamic range = 80 dB for all images. Yellow arrows indicate the wire targets at depths of 45 and 80 mm, which could not be fully resolved due to the limited angular coverage with CW. (D) Comparison of lateral resolution (FWHM, full width at half maximum) as a function of depth for the set of wires located at  $x = 17.6$  mm in (C). (E) Transmission intensity map of 384 conventional ray-line (RyLn) (left) and 384 DW (right) simulated by the Verasonics software package. A sliding active sub-aperture with an  $F$ -number of 2 and a focal depth of 50 mm was used for the RyLn method. The entire aperture of the VLA array (all 384 elements) was used for DW. Top row: Intensity maps of individual transmissions. Bottom row: Summed intensity maps of all 384 transmissions. (F) Standard phantom images acquired by the RyLn method (left) and DW (right). Red arrows indicate the difference in lateral resolution of the wire target. Dynamic range = 65 dB. (G) Lateral resolution as a function of depth for the set of wires located at  $x = 14$  mm in (F).

where  $r$  denotes the focal depth. As the maximum steering angle  $\alpha \in [0, \pi/2]$ ,  $\theta_{\text{DW}} > \theta_{\text{PW}} > \theta_{\text{CW}}$  always holds given the same steering range. We simulated the transmission intensity map in the Verasonics software package with 45 transmissions and a maximal steering angle of 30° using the following four imaging sequences: DW with a virtual source radius of 100 mm, PW, CW with a focal depth of 120 mm, and CW with a focal depth of 80 mm (Fig. 2B). By placing the virtual source behind the array, DW transmission samples a larger angular section than the PW and CW, thus offering a large angular coverage of  $\pm 137.4^\circ$  (Table 1).

In addition to angular coverage, acoustic field homogeneity is crucial to ensure uniform intensity and high contrast across the FOV. We analyzed the acoustic field homogeneity using three metrics: coefficient of variation =  $\sigma/\mu$  (where  $\mu$  is the mean and  $\sigma$  is the

SD of the simulated acoustic intensity), edge-to-center ratio (ECR) =  $\mu_{\text{edge}}/\mu_{\text{center}}$ , and far-to-near-field ratio (FNR) =  $\mu_{\text{far}}/\mu_{\text{near}}$  (Table 1). We found that DW produce a homogeneous acoustic field with a smaller coefficient of variation of 0.39, a higher ECR of 0.67, and a higher FNR of 0.60 compared to PW and CW, indicating a more uniform intensity distribution across the FOV in both lateral and depth directions (Fig. 2B and Table 1).

We acquired images using the four coherent compounding sequences in a standard ultrasound phantom (CIRS Model 040GSE). Images acquired with DW and PW exhibited a nearly depth-independent, uniform brightness distribution. In comparison, CW sequences exhibited higher average transmission intensity near the focal depth but showed a large intensity variation, with a substantial drop near the lateral edges and at greater imaging depths (Fig. 2C). With CW,

wire targets at depths of 45 and 80 mm (yellow arrows) could not be fully resolved due to the limited angular coverage, whereas the DW successfully visualized all wire targets.

We then analyzed the image quality in terms of contrast for hyperechoic cysts and lateral resolution for wire targets in a standard phantom using different imaging sequences. No major differences were observed in contrast ratio (CR), contrast-to-noise ratio (CNR), and generalized contrast-to-noise ratio (gCNR) (19) (Fig. 2C and Table 2). In addition, lateral resolution was similar across the different imaging sequences (Fig. 2D), with some variation in the resolution of the CW sequences near and far from the focus. By placing a tissue-mimicking gelatin layer above the phantom, we further showed that the use of PW and DW with the VLA enhanced the FOV and maintained similar spatial resolution and contrast metrics in the presence of aberration (fig. S1 and table S1). These results confirmed that DW can maintain high image quality while providing a broader FOV.

Although equivalent spatial resolution can be attained with diverging and ray-line methods with commercial probes as described in (20), the use of a large array with DW has unique aspects as the required steering angle is relatively small and the protocol needed to obtain a wide FOV differs. Here, we evaluate the performance of DW with a large-aperture array in comparison to conventional ray-line transmission. Conventional ray-line focusing uses approximately the same number of transmissions as the number of elements, which is 384 in the case of VLA array; therefore, here we also acquired images with 384 DW for comparison. We found that each ray line offered a greater intensity at the focal depth compared to DW, however when summing all transmissions together, the ray-line method generated a spatially variant intensity distribution with lower amplitude near the

focal depth and higher amplitude otherwise (Fig. 2E). Instead, DW produce a uniform acoustic field due to the larger spatial overlap between angular sectors between transmissions given the large activate aperture size. In a standard phantom, the combination of large aperture and DW enhanced lateral resolution substantially across the depth dimension compared to the ray-line method (Fig. 2, F and G).

### Large-aperture array improves human spine imaging

We evaluated the performance of spine imaging using the VLA array compared to a 192-element curvilinear probe that is used clinically (Acuson 6C2, Siemens, Issaquah, WA; 61-mm imaging aperture, center frequency = 4.5 MHz, 90% fractional bandwidth, one-wavelength pitch). The VLA array enhances the image quality substantially in both male (Fig. 3 and fig. S2) and female (fig. S3) human volunteers. In the transverse plane (i.e., horizontal plane that divides the body into superior and inferior sections and is perpendicular to both the sagittal plane and coronal plane), the VLA array maintains lateral resolution in a larger depth range, allowing visualization of deep anatomical structures including the posterior vertebral venous plexus and the spinal canal. Details of the bone structures, especially features deep to the spinous processes, were obscured by acoustic shadowing with the conventional probe but successfully delineated with the VLA array (Fig. 3). Taking advantage of large angular coverage provided by DW transmission, more laterally located structures such as the facets and transverse processes on both sides were visualized with the VLA array. In the longitudinal plane (i.e., sagittal plane, which is vertically oriented and aligned along the body's long axis), the 6C2 probe visualized two vertebrae within the FOV, whereas the VLA array imaged four vertebrae in a single view (figs. S2 and S3). These landmarks can be particularly useful for measuring the vertebrae dimensions in

**Table 1. Evaluation of the angular coverage and transmission field homogeneity using ultrafast imaging sequences.** Field homogeneity metrics are calculated from the simulated transmission intensity using the Verasonics software package.

	DW	PW	CW (120 mm)	CW (80 mm)
Angular coverage (°)	137.4	120	98.7	86.6
Field homogeneity				
Coefficient of variation	0.39	0.54	0.90	0.90
Edge-to-center ratio (ECR)	0.67	0.41	0.19	0.17
Far-to-near-field ratio (FNR)	0.60	0.59	0.36	0.57

**Table 2. Evaluation of contrast metrics using ultrafast imaging sequences in a standard phantom.** Colors correspond to ROIs in Fig. 2C.

Sequence	DW	PW	CW (120 mm)	CW (80 mm)
<i>Hyperechoic Cyst 45 mm (magenta)</i>				
CR (dB)	16.95	16.94	16.63	16.85
CNR	1.78	1.70	1.62	1.64
gCNR	0.92	0.94	0.92	0.92
<i>Hyperechoic Cyst 130 mm (cyan)</i>				
CR (dB)	15.31	16.12	15.61	16.07
CNR	1.41	1.46	1.46	1.46
gCNR	0.86	0.89	0.87	0.89

diagnostics and for determining the target and trajectory of the spinal needle in real-time guidance for interventional procedures.

### Large-aperture array enables lumbar vertebral measurements

We performed *in vivo* imaging on the lumbar and cervical spine of seven healthy volunteers following the protocol approved by the Institutional Review Board (IRB-44593). In all volunteers, the spinal canals were visualized by the VLA array, which enabled quantitative measurements of the lumbar vertebrae (Table 3). The spinal canal depths are defined as the distance from the skin surface to the dorsal and ventral aspects of the spinal canal, and the anterior-posterior

dimension of the spinal canal is defined as the distance between the dorsal and ventral spinal canal. Variations in the size and shape of lumbar vertebrae were observed among volunteers, where larger dimensions of the vertebrae were associated with higher body mass index (BMI) and larger body habitus.

### Nonlinear beamforming improves visualization of details on spine anatomical features

Although the use of short-lag spatial coherence (SLSC) beamforming has been shown to improve visualization of bony anatomical landmarks (21), nonlinear beamforming methods have not been fully investigated for spine imaging. We further evaluated the image

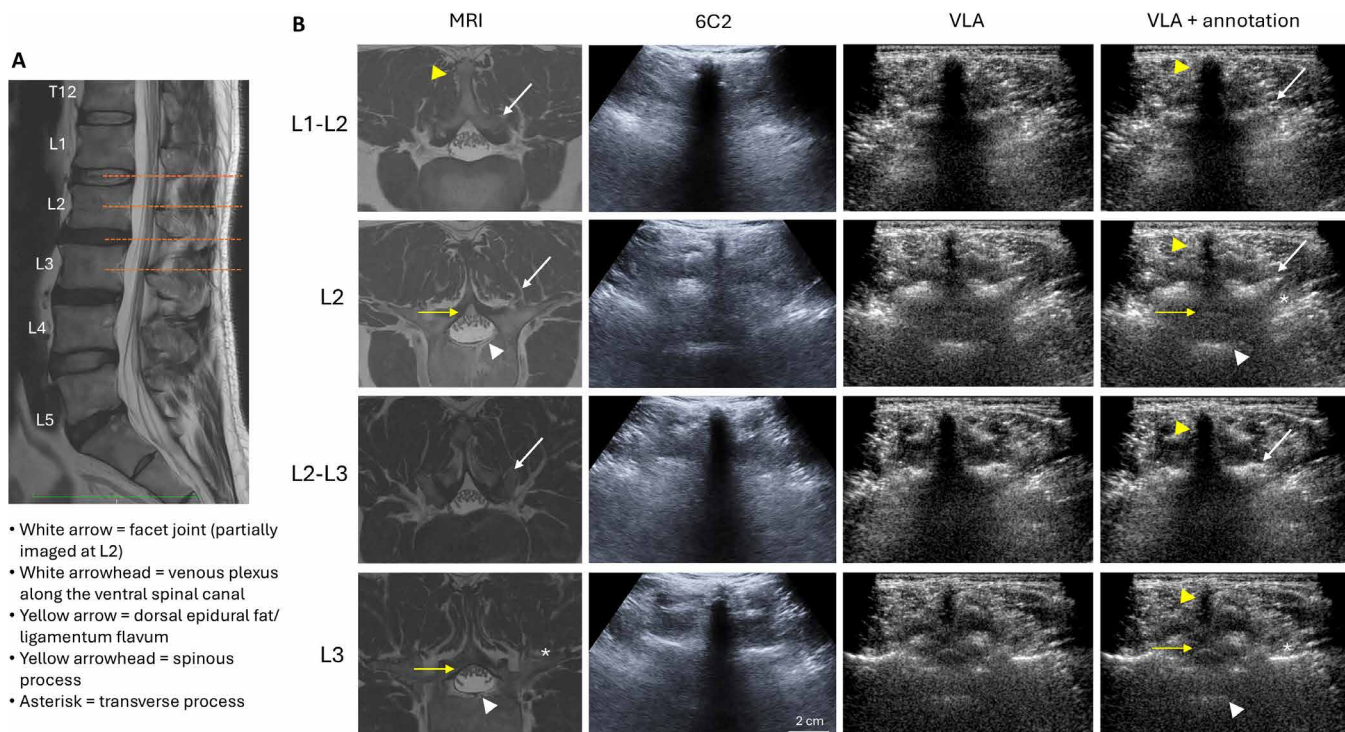


**Fig. 3. Large-aperture array improves the image quality in the human lumbar spine.** (A) Sagittal MRI shows the cross-sectional planes (orange dashed lines) where the ultrasound images were acquired (volunteer #7, male, BMI 26.4). (B) Postprocessed images acquired by the VLA array in comparison to the conventional images and reference MRI in the transverse view.

**Table 3. Lumbar spine measurements from volumetric ultrasound scans of seven healthy human volunteers.** F, female; M, male; std, standard deviation.

Volunteer	Age	Gender	BMI	Spinal canal depth: dorsal (mm)	Spinal canal depth: ventral (mm)	A-P dimension of the spinal canal (mm)
1	27	F	18.0	40.8	55.8	15
2	37	M	24.0	63.8	78	14.2
3	31	F	20.3	45.2	60	14.8
4	39	M	29.0	75.0	93.5	18.5
5	29	F	19.1	36.6	48	11.4
6	40	M	25.0	50.2	62.8	12.6
7	52	M	26.4	45.4	60.2	14.8
Mean ± std	37.4 ± 7.6	–	23.7 ± 3.5	52.0 ± 13.0	66.3 ± 14.9	14.4 ± 2.2

quality improvement using a nonlinear, coherence-factor-weighted delay-and-sum (CF-DAS) beamforming with the VLA array. Different from the standard linear delay-and-sum (DAS), which integrates the acoustic intensity across all channels uniformly, CF-DAS assigns nonlinear weighting factors to suppress side lobes and incoherent signals embedded in the received data (19). We found that the CF-DAS was more robust to acoustic shadowing effects and improved the image quality, especially the visibility of the spinous processes and spinal canal (Fig. 4, A and B). To evaluate the ability to resolve anatomical features of the spine, we analyzed the spatial resolution by taking line profiles across the spine along the lateral (X) and depth (Z) dimensions on human spine images. The line profiles revealed improved resolution and enhanced discrimination of anatomical features using CF-DAS in both depth and lateral dimensions (Fig. 4C). We performed one-way analysis of variance (ANOVA) for statistical analysis and showed that CF-DAS improved the CR, CNR, and gCNR with a  $P$  value  $\leq 0.05$  in 11 of 12 measurements (Fig. 4D).

#### Ultrasound-CT volume coregistration validated the accuracy of ultrasound spine imaging

The lumbar spine structures were successfully acquired by a single volumetric scan for all human volunteers without detectable physiological motion (movie S1). Volumes up to 12 cm by 20 cm by 10 cm (lateral by longitudinal by depth) were acquired within 5 s during a single breath-hold. We used a previously acquired CT scan from one volunteer (#2, 37-year-old male) as a reference to quantitatively evaluate the performance of the volumetric ultrasound scan using the

VLA array. The ultrasound volume and CT volume for the same volunteer were coregistered in three dimensions (3D) and overlaid in blending mode for visualization (Fig. 5, A and B). To evaluate the agreement between measurements, we performed the Bland-Altman analysis in GraphPad (GraphPad Software LLC, San Diego, CA, USA) and showed a 95% agreement between measurements taken from the ultrasound and CT images separately, with all differences falling within the limits of agreement (Fig. 5C and fig. S4), confirming the accuracy of ultrasound volumetric scans with the large-aperture array. The large FOV allowed real-time measurement of the spinous process, facet, interspinous space, interfacet space, and spinal canal depth, which can be useful in interventional guidance.

#### Volumetric spine scan enables 3D rendering of the vertebrae

To demonstrate the feasibility of 3D rendering of spine structure based on ultrasound imaging, we scanned a spine phantom and segmented the spinal bone structure from volumetric ultrasound data based on morphological operations (Fig. 6, A and B). Bland-Altman analysis showed a 95% agreement between measurements from ultrasound images acquired by the VLA array and direct caliper measurements of the spine phantom (Fig. 6C), indicating the accuracy of real-time volumetric ultrasound imaging. One limitation of ultrasound imaging is that the received echoes are obtained as a function of the angle of incidence. At large incident angles, the specular reflection from the bone surface is not received on the 1D probe, resulting in missing fragments in the reconstructed bone structures (e.g., the sides of the spinous processes) (Fig. 6B). To expand the

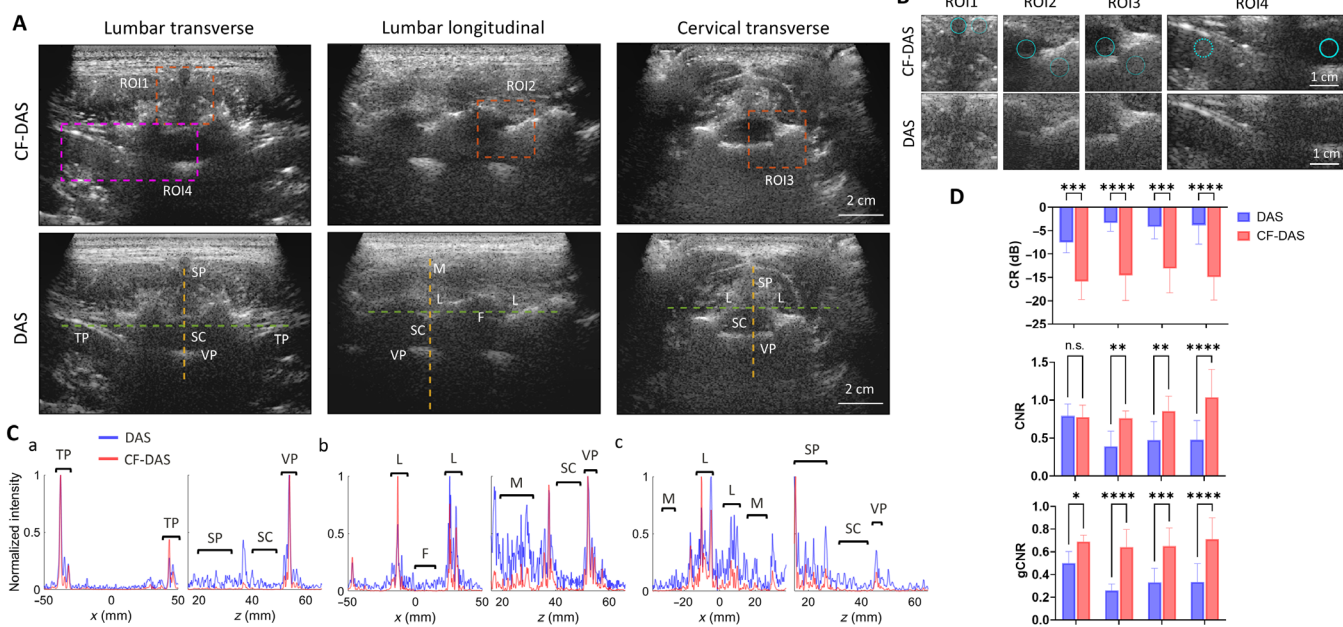


**Fig. 4. Evaluation of spine image quality using linear and nonlinear beamforming.** (A) In vivo spine images from a healthy volunteer using the DAS and CF-DAS beamformer. The dashed lines denote where the line profiles were evaluated (yellow line: axial profile; green line: horizontal profile). TP, transverse process; SP, spinal process; SC, spinal canal; VP, venous plexus; F, facet; L, lamina; M, muscle. Dynamic range = 90 dB for CF-DAS images and 60 dB for DAS images. (B) Magnified view of the four ROIs. ROI1, lumbar spinous process (transverse); ROI2, lumbar facet (longitudinal); ROI3, cervical spinal canal (transverse); ROI4, lumbar spinal canal (transverse). The circular regions denote where the contrast metrics were evaluated (solid line: signal region; dotted line: background region). (C) Line profiles from images in (A) for lumbar spine transverse view (a), lumbar spine longitudinal view (b), and cervical spine transverse view (c). (D) Statistical analysis of image quality metrics in CR (top), CNR (bottom left), and gCNR (bottom right). All data were plotted as the means  $\pm$  SD. not significant (n.s.):  $P > 0.05$ ; \* $P \leq 0.05$ ; \*\* $P \leq 0.01$ ; \*\*\* $P \leq 0.001$ , \*\*\*\* $P \leq 0.0001$ . Raw data used for calculating contrast metrics are provided in table S2.

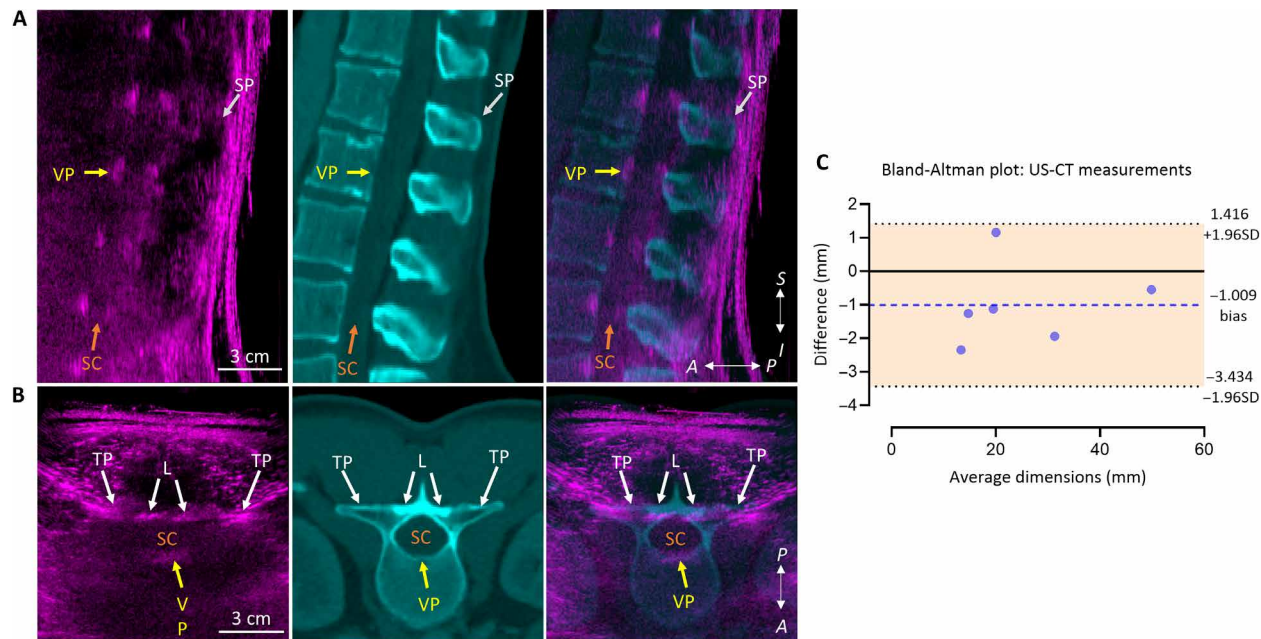


**Fig. 5. Ultrasound-CT comparison.** (A) Cross-sectional images of the lumbar spine in longitudinal view. Left: Ultrasound images. Middle: CT images. Right: Coregistered ultrasound-CT blending images in pseudocolor (cyan: CT; magenta: ultrasound). A-P, anterior-posterior; S-I, superior-inferior. (B) Cross-sectional images of the lumbar spine volume in transverse view. (C) Bland-Altman analysis of the lumbar spine measurements from the ultrasound (US) and CT images. The orange-shaded area indicates the range that falls within the 95% limits of agreement. Details of the measurements are provided in fig. S4. The measured dimensions include interspinous space (superior-inferior), spinous process length (superior-inferior), spinous process length (anterior-posterior), facet length (superior-inferior), interfacet space (superior-inferior), and spinal canal depth (ventral). TP, transverse process; SP, spinal process; SC, spinal canal; VP, venous plexus; L, lamina.

Downloaded from https://www.science.org on July 25, 2025

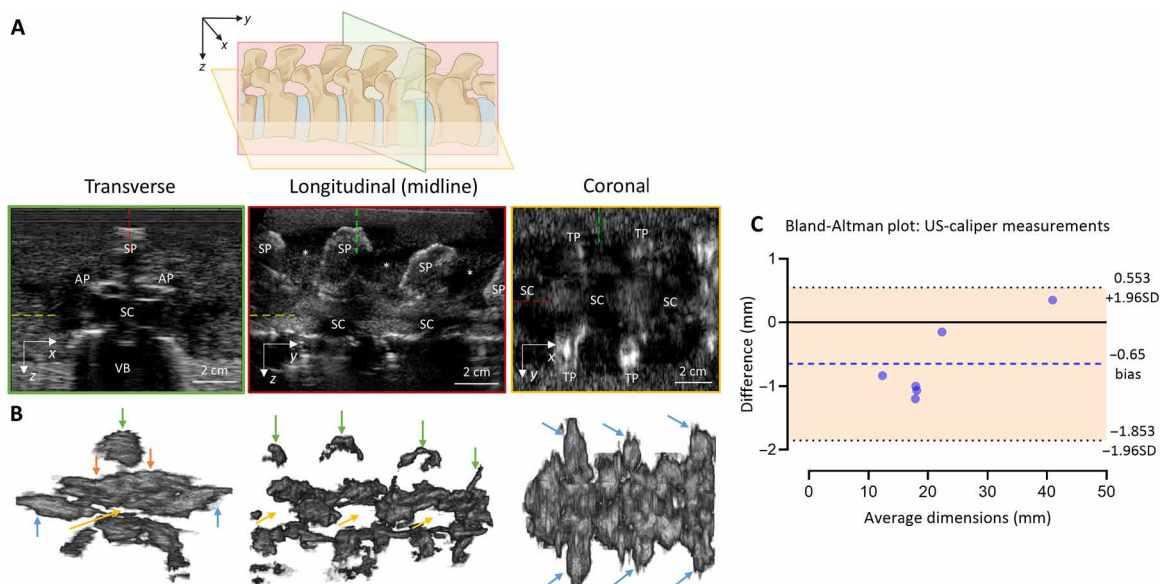


**Fig. 6. Volumetric imaging of a spine phantom.** (A) Cross-sectional images of the spine phantom from one translational scan (scan direction: transverse axis). SP, spinous process; AP, articular process; SC, spinal canal; VB, vertebral body; \*, interspinous space; TP, transverse process. Dynamic range = 100 dB. (B) Segmented bone structures of the spine phantom combined from three translational scans along the lateral axis with the array tilted at -15°, 0°, and 15°. Green arrows: spinous process; yellow arrows: spinal canal; orange arrows: facet; blue arrows: transverse process. (C) Bland-Altman analysis of measurements from ultrasound spine phantom images and direct measurements of the spine phantom using calipers. The orange-shaded area indicates the range that falls within the 95% limits of agreement. The measured dimensions include interspinous space (superior-inferior), spinous process length (superior-inferior), spinous process length (anterior-posterior), facet length (superior-inferior), interfacet space (superior-inferior), and spinal canal depth (ventral).

angular range where echoes can be received, we combined volumetric data from three different angles to improve the 3D segmentation of the spine phantom. For *in vivo* imaging, echoes from peripheral soft tissue also interfere with the specular reflection, making it more challenging to segment the bone structure (fig. S5 and movie S2).

### Large-aperture array facilitates real-time guidance for interventional procedures

We demonstrated the feasibility of ultrasound guidance for interventional procedures using the VLA array in a tissue-mimicking spine phantom. B-mode images were acquired to guide lumbar puncture in a phantom using the 6C2 and the VLA array (Fig. 7A and movie S3). With the 6C2 probe, the needle tip was visible to the level of the facet but was not visible along the deeper structures. In comparison, the spinal needle was visualized and tracked all the way into the spinal canal with the VLA array, confirming the position of the needle in relation to the canal.

We used a microbubble injection to simulate intrathecal administration of contrast (e.g., myelogram). Hyperechoic signals from the injected microbubbles in all three microtubes were identified individually in the spinal canal of the phantom by the VLA array, whereas the 6C2 imaging failed to detect microbubble signal (Fig. 7B). These results demonstrate the utility of the VLA array for real-time interventional guidance.

## DISCUSSION

This study combines a large-aperture ultrasound array with PW and DW transmissions and nonlinear imaging protocols to improve spine visualization across a large FOV at video-rate acquisition. Although the benefits of expanded array apertures and ultrafast imaging sequences have been individually demonstrated, there remains a critical gap in the literature regarding their combined use, particularly for spine imaging. This study demonstrates a real-time panoramic system to image the human spine with ultrasound. The large-aperture array offers improved contrast, resolution, and penetration depth, which cannot be achieved using conventional clinical probes and acquisition systems. The large FOV allows the entire

vertebra to be visualized in the transverse view or three to four vertebrae in the longitudinal view in a single B-mode image, which boosts the intuitive utility of ultrasound with visualization of more anatomical landmarks. The large-aperture array successfully resolved anatomical features at varying depths, including spinous processes (the shallowest target), interspinous space, lamina, facet, transverse processes, and the spinal canal (the deepest target) for all seven human volunteers. Through the combination of the large transducer aperture (8.8 cm) and parallel processing, a large volume was acquired in 5 s during a single breath-hold with sufficient fidelity to segment the bone structure of the spine.

Conventional ultrasound imaging systems typically use either converging beams or scanned focused beams. Previously, Ahmed *et al.* investigated image quality with a VLA array using full synthetic aperture data (11) retrospectively decoded from focused beams by REFOCUS beamforming (20). However, their evaluation focused on a limited FOV of  $\pm 30$  mm. Here, we demonstrate that imaging with the VLA array is synergistic with angular coherent compounding imaging sequences. This combination of capabilities is not available on current commercial systems to the best of our knowledge. Our results showed that DW transmission improves the image quality in terms of resolution, contrast, and field homogeneity in a larger FOV, which offers a favorable and practical solution for human imaging.

Traditionally, ultrasound image quality can be highly operator dependent with a handheld setup (3, 22, 23). In this study, we developed an operator-independent solution for volumetric scanning during spine imaging by using a rigid frame with a conformable interface to facilitate the volumetric acquisition. The current frame design requires the human volunteer to be in the prone posture, but a sealable coupler with a conformable interface is feasible for imaging at other postures as needed while allowing access for intervention. Although volumetric imaging is only demonstrated for the lumbar spine herein, given the limited frame length, the methods can be adapted to cover a larger volume of the spine for the diagnosis of scoliosis (4, 24–28) or real-time treatment guidance around other musculoskeletal structures.

The capacity to visualize the spinal canal in 3D opens up many possibilities for image guidance during spine procedures. Interventions

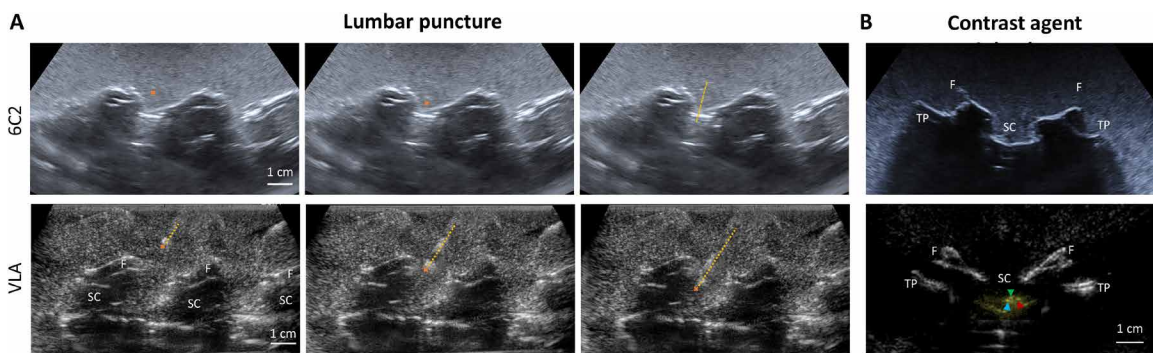


**Fig. 7. Real-time ultrasound guidance for lumbar puncture and contrast agent injection with the VLA array.** (A) A needle was inserted into the spinal canal via the interspinous space during the lumbar puncture procedure. Both the VLA array and the 6C2 system visualized the needle tip in shallow regions above the facet, but the VLA array achieved better visualization following the needle tip and shaft all the way into the spinal canal. The orange X denotes the needle tip, and the yellow dashed line indicates the needle trajectory. (B) The VLA array visualized the injected contrast agent in three microtubes (green, blue, and red arrowheads) embedded in the spine phantom; these were not visible with the 6C2 imaging. Dynamic range = 70 dB for 6C2 images; dynamic range = 100 dB for VLA array images. The bottom image was acquired using a pulse inversion sequence with the VLA array to suppress the static background signal and improve the microbubble visualization. F, facet; SC, spinal canal; TP, transverse process.

such as lumbar puncture, myelogram, therapeutic injection, and biopsy are common procedures for diagnosis and management of not only spinal disorders but also central nervous system diseases. The large-aperture array improves delineation of the spine anatomy and allows real-time 3D segmentation, which can facilitate the procedure and consequently decrease procedure time, failure rate, and/or mistargeting, especially in patients with a large body habitus and more challenging anatomy. Such capability may benefit a broad population of patients as a more accessible alternative to fluoroscopy, CT, or MRI. In the current study, we focused on the structural evaluation of the spine, but this could be further augmented by functional assessment, which is feasible with ultrasound. For instance, high-resolution Doppler imaging can help evaluate paravertebral soft tissue inflammation, infection, spinal neoplasm, and vascular malformations. Future studies will explore strategies to improve the signal-to-noise ratio and sensitivity for Doppler imaging through the spine. Although we only demonstrated the practicality of ultrasound guidance using a spine phantom here, future work will focus on using the large-aperture array for human patient procedures and investigating its performance *in vivo*.

The large-aperture array presented here is a 1D array, and the out-of-plane (elevational) resolution is limited by the physical length of the transducer element in the elevational direction. The 50- to 80-mm focal depth in elevation (with an elevational resolution of 3 mm) is reasonable for human volunteers with large BMI, but for smaller size volunteers or volunteers with lower BMI, a smaller focal depth may be desired to achieve optimal image quality at shallow targets (fig. S3). The focal depth can be reduced by adding a second acoustic lens on the array surface (fig. S6). A 2D array with integrated electronics is under development and would be desirable to achieve optimal elevational focusing at any depth (16, 29).

In conclusion, we improved image quality using a large-aperture ultrasound array with DW transmissions and nonlinear DAS beam-forming methods. Volumetric scans of the spine were demonstrated approaching real time, which enabled measurements and 3D rendering of spine anatomical features. Interventional procedures such as lumbar puncture and contrast agent injection were guided and visualized with ultrasound in a spine phantom. The results support that volumetric and real-time ultrasound using a large-aperture array can better visualize the spine compared to conventional ultrasound and may help supplement CT and MRI in diagnosing and treating various spinal disorders.

## MATERIALS AND METHODS

### Large-aperture array system

The prototype 1D phased array was developed in collaboration with Vermon (Tours, France) with a center frequency of 2.5 MHz, 80% fractional bandwidth, and 384 elements with 0.23-mm pitch (<wavelength/2) in azimuth, resulting in an 88.3-mm imaging aperture. Compared to the clinical probe 6C2, the VLA array improves the lateral resolution substantially by expanding the aperture and reducing the pitch (Fig. 1A). The array has an elevational dimension of 14 mm and an embedded lens with a radius of 65 mm and a sound speed of 1015 m/s, offering an elevational focal depth of 80 mm. To improve focusing for targets in the 50- to 70-mm range, we fabricated an additional lens in-house using silicone rubber (Let's Resin 15A clear silicon, China) with a sound speed of 1000 m/s to achieve a 35-mm radius, reducing the focal depth to 60 mm (fig. S6). The

VLA array is interfaced with three 128-channel connectors and driven by a programmable ultrasound platform that consists of three Vantage 256 Systems (Verasonics Inc., Kirkland, WA) with external clock synchronization to allow simultaneous access of 384 elements. Impedance matching between the electronics and piezo elements was implemented to achieve the optimal bandwidth and transmit-receive efficiency.

### Tissue-mimicking spine phantom

The background substrate of the phantom was prepared by dissolving 3% (w/v) agarose powder (Sigma-Aldrich, St. Louis, MO, USA) in degassed water at 90°C using a magnetic stirrer, offering a sound speed of 1490 m/s at room temperature (30). To mimic biological tissue attenuation, 0.53% silicon carbide (SiC) powder, 0.94% aluminum oxide (3 μm), and 0.88% aluminum oxide (0.3 μm) were mixed with the substrate homogeneously before solidification. A plastic spine model containing L2 to L5 was embedded at the center of the phantom. A rubber sheet with a thickness of ¾ inch (1.905 cm) was placed underneath the plastic spine to absorb reflected acoustic waves from the bottom. For interventional guidance experiments, we embedded three elastomeric tubes (Liveo Silicone Laboratory Tubing, Dupont, Wilmington, DE, USA) with 0.5-mm inner diameter in the spinal canal of the phantom to facilitate the simulation of an intravenous injection procedure (Fig. 1C).

### Image quality evaluation

The contrast metrics were calculated to quantify the image contrast as follows:  $CR = 20 \times \log_{10}(\mu_1/\mu_0)$ ,  $CNR = \frac{|\mu_1 - \mu_0|}{\sqrt{\sigma_1^2 + \sigma_0^2}}$ ,  $gCNR = 1 - \int_{-\infty}^{+\infty} \min \{ p_0(x), p_1(x) \} dx$ , where  $\mu$  and  $\sigma$  denote the

mean and SD, respectively, and  $p(x)$  indicates the probability density function within the region of interest (ROI) (31). Circular ROIs (denoted by 1 in equations) were placed in the target spine structures, whereas background regions (denoted by 0 in equations) were placed in the surrounding background tissue. During the imaging sequence analysis, a tissue-mimicking gelatin layer (Gelatin #0, Humimic Medical, Greenville, SC, USA) with a speed of sound of 1440 m/s was fabricated and placed between the array and the CIRS phantom (1540 m/s) to introduce aberration in the imaging sequence analysis. The gelatin layer was designed to have a rippled surface using random Fourier modes (32), offering a spatially varying thickness range of 20 to 40 mm.

### Human spine imaging protocol

All the human ultrasound imaging was performed following the protocol approved by the Institutional Review Board (IRB-44593). Informed written consent was obtained from all seven volunteers involved in human spine imaging. One of the volunteers (volunteer #7) was diagnosed with mild stenosis and herniation in the lumbar spine. None of the other volunteers had a history of spinal injuries or any treatments affecting the spinal region. The acoustic output of the imaging sequence was calibrated using a needle hydrophone (HNP-0400, Onda Corporation, Sunnyvale, CA, USA). At a focal depth of 60 mm (with the additional lens), the measured mechanical index (MI), spatial-peak temporal-average intensity ( $I_{sptia}$ ), and spatial-peak pulse-average intensity ( $I_{sppa}$ ) were 0.3 and 412 mW/

$\text{cm}^2$  and  $173 \text{ W/cm}^2$ , respectively. All values were below the FDA (Food and Drug Administration) safety limits of  $1.9 \text{ mW/cm}^2$  and  $190 \text{ W/cm}^2$ , respectively.

Single-cycle pulses were transmitted from 45 virtual sources at a radius of 100 mm within a steering range of  $[-30, 30]^\circ$  to coherently form diverging wavefronts at each angle. The frame rate was 50 Hz, and radio-frequency signals were acquired at a sampling frequency of 10 MHz. Uniform rectangular apodization was applied in transmission and reception.

During the imaging session, the volunteers were positioned prone on a horizontal bed. For 2D image acquisition, an operator manually placed the array on the volunteers' back with acoustic gel for coupling and alternated between two orthogonal planes (transverse and longitudinal views) to visualize the spine structures. A previously acquired MRI scan of the lumbar spine from one volunteer (#7, 52-year-old male) was compared with the 2D ultrasound images retrospectively as the anatomical reference.

For the volumetric scan, a coupling frame was placed on the volunteers' lower back and the VLA array was attached to a rigid rail on the frame (Fig. 1B). For each scan, the array was manually translated to collect 150 to 250 frames spanning up to 20 cm. To maximize the acquisition rate, the scan was stored at a frame rate of 50 Hz without reconstruction/display during acquisition (total time within 5 s per scan). The array position was tracked by a rotary encoder (CALT, China) with a spatial resolution of 0.032 mm and captured by an Arduino Nano Board (Arduino, Somerville, MA, USA). Frames in the volume scan were individually beamformed and interpolated along the scan axis with a spacing of 0.2 mm. A sound speed of 1540 m/s was used for image reconstruction.

### Image reconstruction and postprocessing

Both DAS and CF-DAS beamformers were implemented on a GPU (Titan RTX, Nvidia, Santa Clara, CA) with CUDA codes designed in-house, allowing real-time processing (17). The reconstructed images were displayed using MATLAB R2021b (Mathworks, Natick, MA). The average reconstruction time per frame was 0.03 and 0.07 s for DAS and CF-DAS beamformers, respectively.

The image quality achieved by the VLA array was compared to that obtained with the curvilinear probe 6C2. A clinical ultrasound system, Siemens S3000, controlled the curvilinear array and acquired B-mode images using a conventional focused beam sequence. Image postprocessing is used in clinical scanners to improve image quality (e.g., reduce speckle noise and enhance contrast), but the postprocessing techniques vary across manufacturers and are kept proprietary. We processed the raw beamformed images acquired by the VLA array into the approximate clinical-grade images using a standard postprocessing algorithm. Intensity normalization was applied to enhance the contrast of the Gaussian-filtered VLA images, followed by a local Laplacian filter for edge-preserving smoothing. A board-certified neuroradiologist reviewed the postprocessed images to ensure that no anatomical details were lost during image processing.

### Volumetric data analysis and 3D rendering

The CT scan of volunteer #2 offered an in-plane resolution of 0.77 mm by 0.77 mm and a slice thickness of 1.25 mm. Coregistration between the CT and ultrasound volumetric scans was achieved by linear transformation based on anatomical landmarks in 3D Slicer (<http://slicer.org>). The coregistered volumes were blended additively

to analyze the correlation between the two modalities. Six groups of measurements were taken from the ultrasound and CT images separately after coregistration, including the interspinous space width (superior-inferior), spinous process lengths (superior-inferior), spinous process lengths (anterior-posterior), facet lengths (superior-inferior), interfacet space widths (superior-inferior), and spinal canal depths (ventral).

To segment the spinal bone structure from volumetric ultrasound data, ROI masks were first manually drawn to exclude the non-spine pixels from the volume. A 3D Gaussian filter was applied to smooth the volume, followed by a Canny operator to find the boundaries of the bone surface. The connected components near the boundaries were then detected by a MATLAB function bwconncomp. We removed small connected components to suppress non-bony clutter. The segmented 3D volumes were rendered in MATLAB Volume Viewer.

### Simulated interventional procedures

Two simulated interventional procedures were conducted in a spine phantom. First, a lumbar puncture procedure was performed using a 20-gauge needle. Before the needle insertion, the VLA array was placed in the transverse view to determine the required penetration depth of the needle based on the depth of the spinal canal. Then, the VLA array was rotated  $90^\circ$  to the longitudinal view to guide the needle into the spinal canal through interspinous space. As a proof of concept for contrast agent injection with ultrasound guidance, homemade lipid-shelled microbubbles were injected into the three elastomeric tubes embedded in the phantom, and B-mode ultrasound images were acquired using the VLA array pre- and postinjection. The microbubbles have a similar size distribution to the clinically used agent (1 to  $2 \mu\text{m}$  at a concentration of  $1.2 \times 10^8$  microbubbles/ml) (33).

### Supplementary Materials

**The PDF file includes:**

Figs. S1 to S6

Tables S1 and S2

Legends for movies S1 to S3

**Other Supplementary Material for this manuscript includes the following:**

Movies S1 to S3

### REFERENCES AND NOTES

- N. Boos, M. Aeby, Eds., *Spinal Disorders: Fundamentals of Diagnosis and Treatment* (Springer Berlin, 2009), vol. 30, 1165 pp.
- K. Mataki, M. Koda, Y. Shiba, H. Kumagai, K. Nagashima, K. Miura, H. Noguchi, T. Funayama, T. Abe, M. Yamazaki, Successful visualization of dynamic change of lumbar nerve root compression with the patient in both upright and prone positions using dynamic digital tomosynthesis-radiography in patients with lumbar foraminal stenosis: An initial report of three cases. *J. Clin. Neurosci.* **62**, 256–259 (2019).
- N. J. Soni, R. Franco-Sadud, D. Schnobrich, R. Dancel, D. M. Tierney, G. Salame, M. I. Restrepo, P. McHardy, Ultrasound guidance for lumbar puncture. *Neurol. Clin. Pract.* **6**, 358–368 (2016).
- C.-W. J. Cheung, G.-Q. Zhou, S.-Y. Law, T.-M. Mak, K.-L. Lai, Y.-P. Zheng, Ultrasound volume projection imaging for assessment of scoliosis. *IEEE Trans. Med. Imaging* **34**, 1760–1768 (2015).
- H.-Y. Zeng, E. Lou, S.-H. Ge, Z.-C. Liu, R. Zheng, Automatic detection and measurement of spinous process curve on clinical ultrasound spine images. *IEEE Trans. Ultrason. Ferroelectr. Freq. Control* **68**, 1696–1706 (2021).
- H.-E. Gueziri, C. Santaguida, D. L. Collins, The state-of-the-art in ultrasound-guided spine interventions. *Med. Image Anal.* **65**, 101769 (2020).
- T. L. Szabo, Ed., “Chapter 6: Beamforming” in *Diagnostic Ultrasound Imaging: Inside Out (Second Edition)* (Academic Press, 2014), pp. 167–207.
- P.-J. S. Tsai, M. Loichinger, I. Zalud, Obesity and the challenges of ultrasound fetal abnormality diagnosis. *Best Pract. Res. Clin. Obstet. Gynaecol.* **29**, 320–327 (2015).

9. M. Klysik, S. Garg, S. Pokharel, J. Meier, N. Patel, K. Garg, Challenges of imaging for cancer in patients with diabetes and obesity. *Diabetes Technol. Ther.* **16**, 266–274 (2014).
10. L. Peralta, A. Gomez, Y. Luan, B.-H. Kim, J. V. Hajnal, R. J. Eckersley, Coherent multi-transducer ultrasound imaging. *IEEE Trans. Ultrason. Ferroelectr. Freq. Control* **66**, 1316–1330 (2019).
11. R. Ahmed, J. Foiret, K. Ferrara, G. E. Trahey, Large-array deep abdominal imaging in fundamental and harmonic mode. *IEEE Trans. Ultrason. Ferroelectr. Freq. Control* **70**, 406–421 (2023).
12. N. J. Pettersson, M. R. H. M. van Sambeek, F. N. van de Vosse, R. G. P. Lopata, Enhancing lateral contrast using multi-perspective ultrasound imaging of abdominal aortas. *Ultrasound Med. Biol.* **47**, 535–545 (2021).
13. N. Bottenus, W. Long, M. Morgan, G. Trahey, Evaluation of large-aperture imaging through the ex vivo human abdominal wall. *Ultrasound Med. Biol.* **44**, 687–701 (2018).
14. R. Wodnicki, H. Kang, D. Li, D. N. Stephens, H. Jung, Y. Sun, R. Chen, L.-M. Jiang, N. E. Cabrera-Munoz, J. Foiret, Q. Zhou, K. W. Ferrara, Highly integrated multiplexing and buffering electronics for large aperture ultrasonic arrays. *BME Front.* **2022**, 9870386 (2022).
15. J. Foiret, X. Cai, H. Bendjador, E. Y. Park, A. Kamaya, K. W. Ferrara, Improving plane wave ultrasound imaging through real-time beamformation across multiple arrays. *Sci. Rep.* **12**, 13386 (2022).
16. H. Bendjador, J. Foiret, R. Wodnicki, D. N. Stephens, Z. Krut, E.-Y. Park, Z. Gazit, D. Gazit, G. Pellet, K. W. Ferrara, A theranostic 3D ultrasound imaging system for high resolution image-guided therapy. *Theranostics* **12**, 4949–4964 (2022).
17. E.-Y. Park, X. Cai, J. Foiret, H. Bendjador, D. Hyun, B. Z. Fite, R. Wodnicki, J. J. Dahl, R. D. Boutin, K. W. Ferrara, Fast volumetric ultrasound facilitates high-resolution 3D mapping of tissue compartments. *Sci. Adv.* **9**, eadg8176 (2023).
18. W. F. Walker, G. E. Trahey, The application of k-space in pulse echo ultrasound. *IEEE Trans. Ultrason. Ferroelectr. Freq. Control* **45**, 541–558 (1998).
19. P.-C. Li, M.-L. Li, Adaptive imaging using the generalized coherence factor. *IEEE Trans. Ultrason. Ferroelectr. Freq. Control* **50**, 128–141 (2003).
20. N. Bottenus, Recovery of the complete data set from focused transmit beams. *IEEE Trans. Ultrason. Ferroelectr. Freq. Control* **65**, 30–38 (2018).
21. E. A. Gonzalez, A. Jain, M. A. L. Bell, Combined ultrasound and photoacoustic image guidance of spinal pedicle cannulation demonstrated with intact ex vivo specimens. *IEEE Trans. Biomed. Eng.* **68**, 2479–2489 (2021).
22. M. A. Peterson, D. Pisupati, T. W. Heyming, J. A. Abele, R. J. Lewis, Ultrasound for routine lumbar puncture. *Acad. Emerg. Med.* **21**, 130–136 (2014).
23. J. T. Nomura, S. J. Leech, S. Shenbagamurthy, P. R. Sierzenski, R. E. O'Connor, M. Bollinger, M. Humphrey, J. A. Gukhool, A randomized controlled trial of ultrasound-assisted lumbar puncture. *J. Ultrasound Med.* **26**, 1341–1348 (2007).
24. S. L. Weinstein, L. A. Dolan, J. C. Cheng, A. Danielsson, J. A. Morcuende, Adolescent idiopathic scoliosis. *Lancet* **371**, 1527–1537 (2008).
25. C.-W. J. Cheung, G.-Q. Zhou, S.-Y. Law, K.-L. Lai, W.-W. Jiang, Y.-P. Zheng, Freehand three-dimensional ultrasound system for assessment of scoliosis. *J. Orthop. Translat.* **3**, 123–133 (2015).
26. Y.-P. Zheng, T. T.-Y. Lee, K. K.-L. Lai, B. H.-K. Yip, G.-Q. Zhou, W.-W. Jiang, J. C.-W. Cheung, M.-S. Wong, B. K.-W. Ng, J. C.-Y. Cheng, T.-P. Lam, A reliability and validity study for Scolioscan: A radiation-free scoliosis assessment system using 3D ultrasound imaging. *Scoliosis Spinal Disord.* **11**, 13 (2016).
27. S. Song, H. Chen, C. Li, E. Lou, L. H. Le, R. Zheng, Assessing bone quality of the spine in children with scoliosis using the ultrasound reflection frequency amplitude index method: A preliminary study. *Ultrasound Med. Biol.* **48**, 808–819 (2022).
28. K. K.-L. Lai, T. T.-Y. Lee, H. H.-T. Lau, W. C.-W. Chu, J. C.-Y. Cheng, R. M. Castelein, T. P. C. Schlösser, T.-P. Lam, Y.-P. Zheng, Monitoring of curve progression in patients with adolescent idiopathic scoliosis using 3-D ultrasound. *Ultrasound Med. Biol.* **50**, 384–393 (2024).
29. R. Wodnicki, H. Bendjador, H. Kang, J. Foiret, C. Notard, Q. Zhou, K. W. Ferrara, “Row-Multiplexed 1,024 Element Large Aperture Array for Electronic Scanning in Elevation,” in *2022 IEEE International Ultrasonics Symposium (IUS)* (IEEE, 2022), pp. 1–4.
30. R. Monteiro Souza, M. K. M. de Assis, R. Pereira Barreto da Costa-Félix, A. V. Alvarenga, Speed of sound in the IEC tissue-mimicking material and its maintenance solution as a function of temperature. *Ultrasonics* **118**, 106564 (2022).
31. A. Rodriguez-Molares, O. M. H. Rindal, J. D'hooge, S.-E. Måsøy, A. Austeng, M. A. Lediju Bell, H. Torp, The generalized contrast-to-noise ratio: A formal definition for lesion detectability. *IEEE Trans. Ultrason. Ferroelectr. Freq. Control* **67**, 745–759 (2020).
32. A. T. Peek, C. Hunter, W. Kreider, T. D. Khokhlova, P. B. Rosnitskiy, P. V. Yuldashev, O. A. Sapozhnikov, V. A. Khokhlova, Bilayer aberration-inducing gel phantom for high intensity focused ultrasound applications. *J. Acoust. Soc. Am.* **148**, 3569–3580 (2020).
33. N. McDannold, N. Vykhotseva, K. Hyynnen, Use of ultrasound pulses combined with Definity® for targeted blood-brain barrier disruption: A feasibility study. *Ultrasound Med. Biol.* **33**, 584–590 (2007).

#### Acknowledgments

**Funding:** This work was supported by the National Institute of Health grants R01CA271309 and R01EB033967 (K.W.F.). **Author contributions:** Conceptualization: N.L., J.F., B.C.Y., and K.W.F. Methodology: N.L., J.F., and Y.G. Investigation: N.L., J.F., and Y.G. Visualization: N.L. Supervision: B.C.Y. and K.W.F. Writing—original draft: N.L. Writing—review and editing: N.L., J.F., Y.G., B.C.Y., and K.W.F. **Competing interests:** The authors declare that they have no competing interests. **Data and materials availability:** All data needed to evaluate the conclusions in the paper are present in the paper and/or the Supplementary Materials.

Submitted 30 January 2025

Accepted 25 June 2025

Published 25 July 2025

10.1126/sciadv.adw2601